Cell Reports
Physical Science

Article

High-performance thermoacoustically driven triboelectric nanogenerator for autonomous wireless monitoring

Graphical abstract

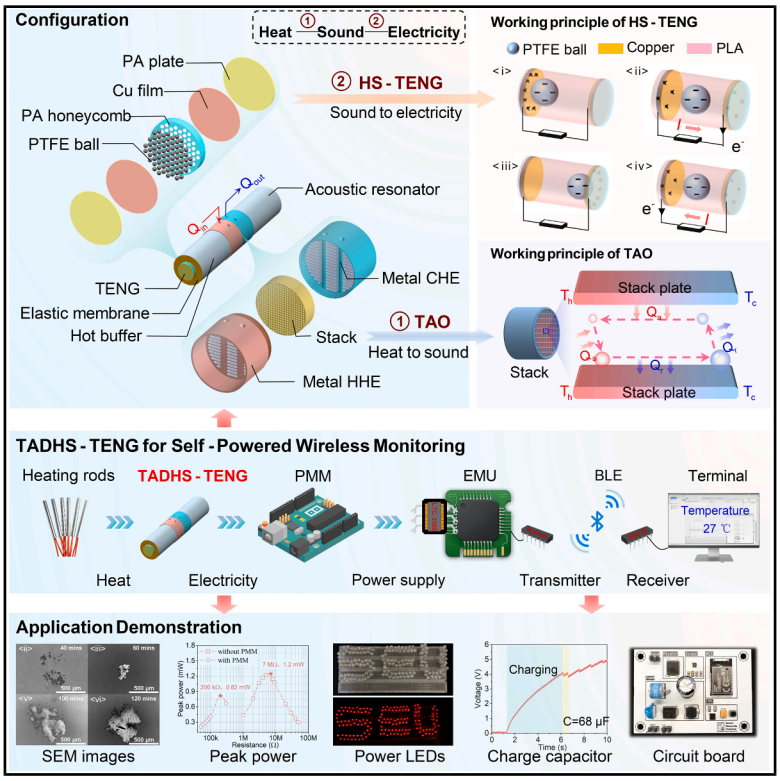

Highlights

- Thermoacoustically driven honeycomb-structured TENG converts heat into electricity
- Achieve a maximum voltage of 124 V and a peak current of 15.82 μA
- Achieve a maximum charge transfer of 50.54 nC and a peak power of 1.2 mW
- Power more than 300 LEDs and a custom-designed wireless temperature sensor node

Authors

Geng Chen (陈庚), Yawei Wang (王雅巍), Shancheng Tao (陶山城), ..., Junlei Wang (王军雷), Guobiao Hu (胡国标), Aidong Deng (邓艾东)

Correspondence

guobiaohu@hkust-gz.edu.cn

In brief

Chen et al. report a thermoacoustically driven honeycomb-structured triboelectric nanogenerator capable of converting low-grade thermal energy into electricity. The device successfully powers more than 300 LEDs and a custom-designed wireless temperature sensor node, demonstrating its significant potential for heat-driven, self-powered monitoring in distributed IoT and industrial sensing systems.

Chen et al., 2026, Cell Reports Physical Science 7, 103214
April 15, 2026
https://doi.org/10.1016/j.xcrp.2026.103214

CellPress

Cell Reports
Physical Science

CellPress
OPEN ACCESS

Article

High-performance thermoacoustically driven triboelectric nanogenerator for autonomous wireless monitoring

Geng Chen (陈庚),[1] Yawei Wang (王雅巍),[2] Shancheng Tao (陶山城),[1,3] Jiawen Xu (徐佳文),[4] Lihua Tang (汤丽华),[5] Junlei Wang (王军雷),[6] Guobiao Hu (胡国标),[2,7,*] and Aidong Deng (邓艾东)[1]

[1]National Engineering Research Center of Power Generation Control and Safety, School of Energy and Environment, Southeast University, Nanjing 210096, China
[2]Internet of Things Thrust, The Hong Kong University of Science and Technology (Guangzhou), Nansha, Guangzhou, Guangdong 511400, China
[3]China United Engineering Corporation Limited, Hangzhou, Zhejiang 310052, China
[4]School of Instrument Science and Engineering, Southeast University, Nanjing 210096, China
[5]Department of Mechanical and Mechatronics Engineering, The University of Auckland, 5 Grafton Road, Auckland 1010, New Zealand
[6]School of Mechanical and Power Engineering, Zhengzhou University, Zhengzhou 450001, China
[7]Lead contact
*Correspondence: guobiaohu@hkust-gz.edu.cn
https://doi.org/10.1016/j.xcrp.2026.103214

SUMMARY

Harvesting low-grade heat offers a promising strategy for sustainable power generation. However, existing thermoacoustic energy harvesters often suffer from low electrical output and limited practical applicability. Here, we report a thermoacoustically driven honeycomb-structured triboelectric nanogenerator (TADHS-TENG) capable of converting heat into electricity and directly powering wireless sensors. The TADHS-TENG integrates a thermoacoustic oscillator with an elastically suspended rolling-ball TENG. It achieves a maximum voltage of 124 V, a peak current of 15.82 μA, a maximum charge transfer of 50.54 nC, and a peak power of 1.2 mW, outperforming previously reported thermoacoustically driven TENGs. By incorporating a power management circuit and an energy storage module, the TADHS-TENG is capable of continuously driving a Bluetooth-enabled temperature sensor that transmits data to the cloud without reliance on external power sources. These results demonstrate the feasibility of heat-driven, self-powered, wireless monitoring and underscore the significant potential of thermoacoustically driven TENGs for driving low-power electronics in real-world environments.

INTRODUCTION

The increasing global energy demand and escalating environmental challenges, such as greenhouse gas emissions and climate change, have intensified the pursuit of clean and renewable energy technologies.[1] Thermal energy harvesting offers a viable route for converting low-grade heat sources (such as solar, geothermal, and industrial waste heat) into mechanical or electrical energy. While organic Rankine cycle (ORC) systems are widely used for this purpose due to their ability to operate with low-boiling-point working fluids, their practical deployment is often constrained by issues related to toxic or flammable fluids, high manufacturing costs, and limited scalability. Consequently, alternative thermal energy harvesting methods, including thermoelectric, pyroelectric, thermionic, thermomagnetic, and thermoacoustic technologies, have attracted increasing attention (see Figure S1 in the supplemental information). Among them, thermoacoustic technology stands out because of its simple structure with few or no moving parts, low maintenance requirements, environmentally benign working fluids, and broad heat source applicability.[2–4] The thermoacoustic technology operates on the thermoacoustic effect, which results from the interaction between an oscillatory working fluid and a solid porous material, such as a stack or regenerator.[5–7] Based on the thermoacoustic effect, thermoacoustic engines (TAEs) or thermoacoustic oscillators (TAOs) can be developed to convert heat into acoustic energy.[8–10] The TAEs or TAOs can be further integrated with acoustic-to-electric transducers, thereby forming thermoacoustic power generators (TAPGs) that can convert heat into electricity.[11–13]

Various types of acoustic-to-electric transducers have been adopted in developing TAPGs, with the most commonly used being those based on the electromagnetic effect, such as linear alternators and loudspeakers.[14] While linear alternators offer high electrical output, they are very bulky and costly. Conversely, loudspeakers are more cost-effective, but their power output and efficiency are limited by the fragile cones. In addition to these two types of electromagnetic acoustic-to-electric transducers,

recent studies have explored the integration of piezoelectric elements into miniaturized thermoacoustic systems.[15–17] Wekin et al.[18] first developed a simplified mathematical model to study the influences of piezoelectric transducer parameters on the onset temperature difference and natural frequency of a standing-wave TAE. In their study, a piezoelectric transducer was placed at the end of the thermoacoustic resonator, leading to a thermoacoustic-piezoelectric (TAP) energy harvester. Subsequently, Smoker et al.[19] designed a TAP prototype for thermal energy harvesting. Their experimental results showed that given a heat input of 44.82 W, the device produced a root mean square (RMS) voltage of 0.9 V and an RMS power of 0.128 mW. Following this, Zhao[20] developed a convection-driven Rijke-Zhao TAP energy harvester. It achieved an RMS output power of 0.21 mW, which was 60% higher than that in the study by Smoker et al.[19] While the introduction of piezoelectric transducers has provided a possible solution for designing small-scale TAPs, the brittleness and poor durability of piezoelectric materials significantly limit the lifespan of thermoacoustic systems.

In light of the aforementioned limitations of piezoelectric transducers, a growing body of research has focused on using triboelectric nanogenerators (TENGs) as a promising alternative for converting mechanical energy into electrical energy.[21–23] TENGs have garnered significant interest due to their advantages, including low material costs,[24] lightweight design,[25] ease of fabrication,[26] high flexibility,[27] and exceptional power density.[28–30] These characteristics make TENGs particularly suitable for a wide range of energy harvesting applications, including wind energy,[31–33] water-wave energy,[34–36] acoustic energy,[37–39] marine energy,[40] and low-grade thermal energy utilization.[41] Generally, TENGs operate in one of the four modes: contact-separation,[42] lateral sliding,[43–45] single-electrode,[46] and freestanding triboelectric layer modes.[47–49] In 2017, Zhu et al.[50] developed a thermoacoustically driven triboelectric nanogenerator (TA-TENG) for thermal energy harvesting. Their TA-TENG integrated a standing-wave TAE with a contact-separation mode TENG, producing a maximum output voltage of 10 V and a peak output power of 0.008 μW. Following Zhu's study,[50] Ahmed et al.[51] conducted numerical and theoretical analyses of the dynamic behavior of TA-TENGs. Using finite element modeling (FEM) and electrical analogy approaches, they optimized the performance of TA-TENGs, resulting in a peak voltage and current of 11.2 V and 0.025 μA, which were in good agreement with experimental results. More recently, Zhu et al.[52] proposed a thermoacoustically driven, liquid-metal-based TENG that operates without solid moving parts. The TENG worked in the contact-separation mode and produced a maximum output voltage of 15 V. Although previous studies have demonstrated the feasibility of TA-TENGs for converting heat into electricity, most reported designs operate in the contact-separation mode, and their performance remains substantially lower than that of other TENG configurations (such as water-cup TENGs [WC-TENGs],[53] all-foam TENGs [AF-TENGs], [54] and Faraday-cage-enabled [FC-TENGs][55]), which limit their practical applications. Consequently, it is imperative to explore TENGs employing alternative or hybrid working modes to more efficiently harvest the acoustic energy generated by thermoacoustic engines.

In this study, we present an innovative TENG, termed TADHS-TENG (short for thermoacoustically driven honeycomb-structured triboelectric nanogenerator), for thermal energy harvesting. As its name suggests, the TADHS-TENG integrates a honeycomb-structured triboelectric nanogenerator (HS-TENG) with a TAO through an elastic membrane coupling, enabling efficient thermal-to-electric energy conversion. Unlike previously reported rigidly coupled thermoacoustic-TENG architectures, the elastic membrane introduces an additional mechanical degree of freedom and a buffering effect, resulting in a tunable dynamic response that actively regulates the rolling motion of the ball units within the honeycomb structure. This elastic-coupling-enabled regulation allows the rolling amplitude, contact frequency, and contact force to be effectively tailored, thereby substantially enhancing triboelectric energy-harvesting performance. By systematically optimizing key structural and mechanical parameters of the TADHS-TENG, including the TENG diameter, the tensile strain of the elastic membrane, and the thermoacoustic tube length, the electrical output performance is significantly improved, reaching levels beyond those of previous thermoacoustic-driven TENGs. Moreover, the time-dependent evolution of the electrical output is investigated and directly correlated with microstructural modifications of the electrode surface induced by continuous rolling contact. This combined electrical and microstructural analysis provides new mechanistic insights into the interfacial charge generation and transfer processes governing the long-term energy conversion behavior of rolling-ball-mode TENGs. Furthermore, to showcase the practical potential of our design, we demonstrate the use of the developed TADHS-TENG to power a specially designed wireless temperature sensing node. In the custom-designed circuit board of this node, the electricity generated by the TADHS-TENG is first regulated and stored in a capacitor via a power modulation module (PMM), then managed by an energy management module (EMM). Therefore, the developed TADHS-TENG enables the wireless temperature sensor to operate autonomously, powered solely by the harvested thermal energy. The findings of this study highlight the great potential of the TADHS-TENG for thermal energy harvesting and underscore its prospects for the development of heat-driven self-powered wireless sensing systems.

RESULTS

System design and working mechanism of the TADHS-TENG

The TADHS-TENG proposed in this study is a sophisticated system for harvesting thermal energy, capable of converting it into mechanical energy and then into electrical energy. Figure 1A illustrates various application scenarios for the TADHS-TENG, which harnesses heat from diverse sources, such as locomotive engines, train braking systems, exhaust gases, steam pipelines, and open flames. The generated electricity, in turn, powers on-site railway signal lights, monitoring sensors for engines and pipeline systems, and low-power electronic devices in daily life. As depicted in Figures 1B and S2 in the supplemental information, the TADHS-TENG is primarily composed of two main components: a TAO and an HS-TENG. The TAO converts

Please cite this article in press as: Chen et al., High-performance thermoacoustically driven triboelectric nanogenerator for autonomous wireless monitoring, Cell Reports Physical Science (2026), https://doi.org/10.1016/j.xcrp.2026.103214

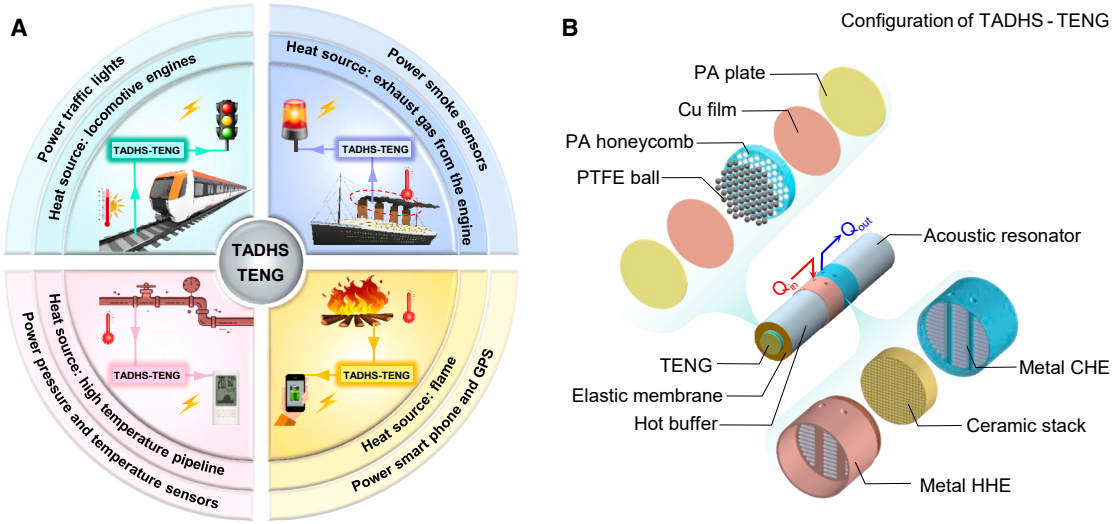

Figure 1. Application scenarios and structural configuration of the proposed TADHS-TENG

(A) Illustration of the TADHS-TENG applied to harvest various heat sources, including railway trains (e.g., engine blocks and braking systems), exhaust gas outlets from ships or vehicles, industrial steam pipelines, and open flames (e.g., from campfires or industrial burners) to power traffic signal lights, monitoring sensors, and low-power electronics.

(B) Structural configuration of the TADHS-TENG, comprising a thermoacoustic oscillator (TAO) and a honeycomb-structured TENG (HS-TENG).

thermal energy into acoustic energy. It consists of several key elements: (1) a pair of aluminum-alloy heat exchangers (namely, a hot heat exchanger [HHE] and a cold heat exchanger [CHE]) serving as the heat source and sink, respectively; (2) a porous ceramic stack sandwiched between the HHE and CHE to facilitate thermal-acoustic energy conversion; (3) an acoustic resonator with its left end connected to the CHE and right end open to the surroundings, functioning as a waveguide for acoustic wave propagation; and (4) a hot buffer with its right end connected to the HHE and left end sealed with an elastic membrane. The HS-TENG, affixed to the surface of the elastic membrane, converts the acoustic energy generated by the TAO into electricity. It consists of a polylactic acid (PLA) honeycomb frame with internal tunnels, polytetrafluoroethylene (PTFE) balls playing the role of electronegative triboelectric layers, copper films acting as electrode layers, and a pair of PLA substrate plates. Each internal tunnel of the honeycomb frame houses a PTFE ball. The honeycomb frame is sandwiched between the two PLA substrate plates, each affixed with a copper film. The entire device is encapsulated with a polyimide (PI) tape to enhance its durability and reliability. The detailed geometrical dimensions of the TADHS-TENG are provided in Figure S3 and Table S2 in the supplemental information.

Figure 2A illustrates the working mechanism of a quarter-wavelength standing-wave TAO. Driven by the temperature gradient across the parallel plate stack, the near-wall gas parcel between the plates contracts and expands while exchanging heat with the nearby plates, thereby forming a thermodynamic cycle. The thermodynamic processes[56] are as follows: (1) As the gas parcel moves from the cold end (T_c) to the hot end (T_h), it absorbs heat from the stack plates. During this process, the gas is compressed, resulting in a rise in its temperature. (2) As the gas remains in thermal contact with the plates, its temperature continues to increase and reaches its maximum before the gas parcel starts to move to the cold end. (3) As the gas parcel moves from the hot end to the cold end, it releases heat to the stack plates, resulting in a decrease in temperature and an increase in volume. (4) The gas temperature continues to decrease due to the imperfect thermal contact with the plates and reaches a minimum before the parcel begins to move to the hot end. As this thermodynamic cycle repeats continuously, thermal energy is converted into acoustic energy. As illustrated in Figure 2A, the gas pressure and volume change periodically, forming a closed elliptical loop on the pressure-volume (p-V) diagram, with the enclosed area representing the acoustic power (ΔW) generated in this process.

According to the first law of thermodynamics, ΔW can be expressed as,

$$\Delta W = Q_a - Q_r, \qquad \text{(Equation 1)}$$

where Q_a and Q_r stand for the heat absorbed from and released to the stack plates, respectively. It is worth noting that this thermodynamic cycle differs from the Stirling cycle since the period of the thermodynamic cycle is determined by the natural frequency of the TAO rather than the forced frequency of an external drive. This unique feature enables thermoacoustic systems to achieve energy conversion without any moving mechanical components, thereby enhancing their reliability and durability.

The acoustic power W can also be described as follows[3]:

$$W = \frac{\omega}{2\pi}\oint pdV = \frac{1}{2}|p_1||U_1|\cos\theta, \qquad \text{(Equation 2)}$$

where $U_1 = dV/dt$ denotes the volume flow rate, ω is the angular frequency, and θ represents the phase difference. The subscript 1 denotes first-order fluctuations of acoustic pressure and

Please cite this article in press as: Chen et al., High-performance thermoacoustically driven triboelectric nanogenerator for autonomous wireless monitoring, Cell Reports Physical Science (2026), https://doi.org/10.1016/j.xcrp.2026.103214

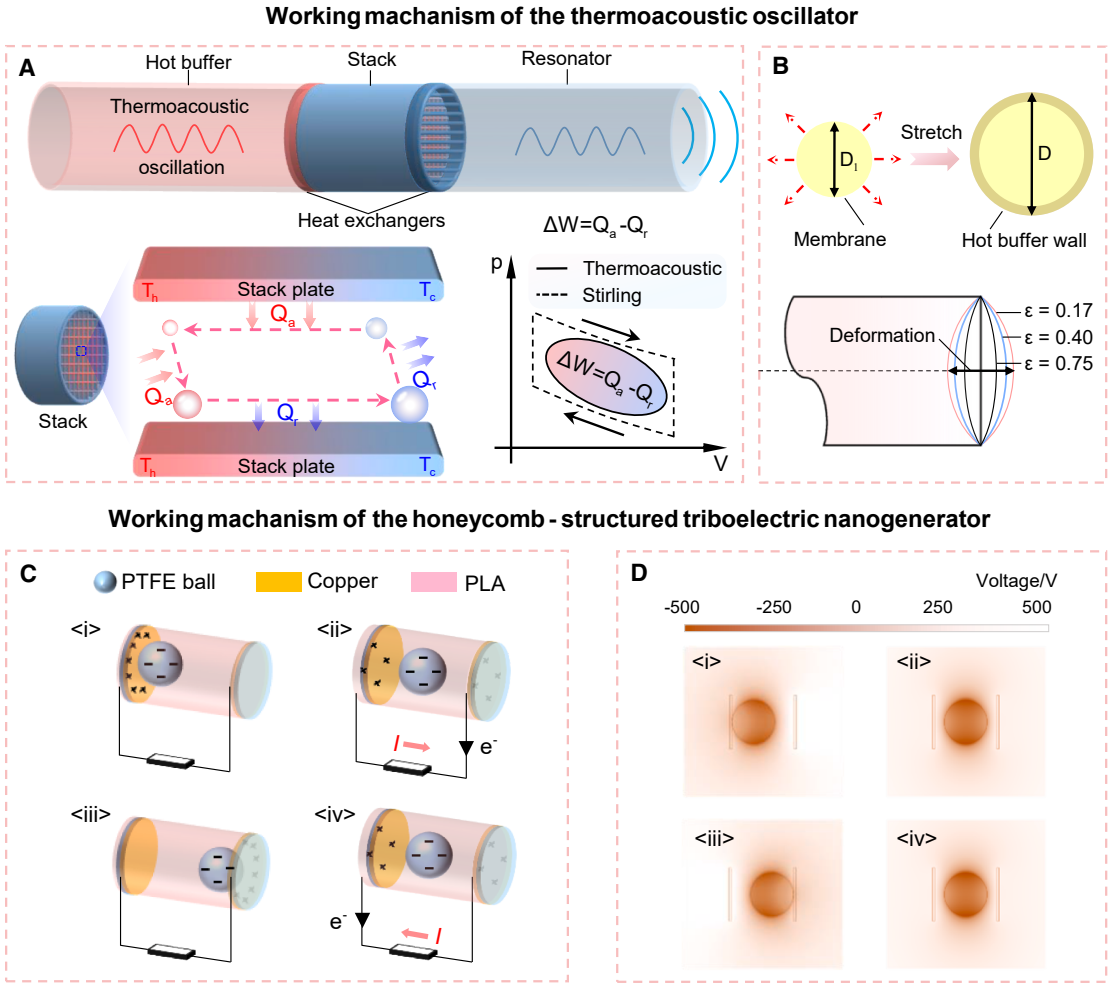

Figure 2. Working mechanism of the TADHS-TENG

(A) The thermodynamic cycle experienced by the gas parcel within the stack of the thermoacoustic oscillator.

(B) Schematic of the elastic membrane under different tensile strains, where D0 and D denote the original and stretched diameters, respectively, and ε represents the corresponding tensile strain.

(C) Conceptual illustration of the working principle of the HS-TENG.

(D) Simulated electrostatic field distribution of the HS-TENG at different operation stages using COMSOL Multiphysics.

volume flow rate oscillations. Figure S4 in the supplemental information illustrates the axial distributions of acoustic pressure and velocity amplitudes within a standing-wave TAO. A standing wave pattern is observed, marked by a pressure antinode (velocity node) at the closed end and a pressure node (velocity antinode) at the open end. Notably, the acoustic power output is strongly influenced by the phase difference θ between p_1 and U_1. Specifically, the acoustic power W becomes zero when θ is 90°, indicating that a purely standing wave does not produce net acoustic power. In practical standing-wave TAOs, θ typically ranges from 85° to 95°. A non-zero acoustic power is primarily attributed to the traveling wave component (although not dominant).

Since a pressure antinode is located at the closed end, we directly couple the HS-TENG to the left end of the hot buffer through an elastic membrane. This elastic membrane deforms in response to pressure oscillations, thereby driving the HS-TENG attached to its surface. As shown in Figure 2B, the diameter of the elastic membrane in its relaxed state is D_0. It is stretched to a diameter of D to seal the left end of the hot buffer. Therefore, the tensile strain ε of the membrane can be expressed as,

$$\varepsilon = \frac{D - D_0}{D_0}. \quad \text{(Equation 3)}$$

A larger ε indicates an increased membrane stiffness and a reduced deformation in response to the same pressure oscillations.

Figure 2C illustrates the material composition and operating mechanism of the HS-TENG. The external structure of the TENG is fabricated from PLA using additive manufacturing techniques. PTFE microspheres are selected as the

Please cite this article in press as: Chen et al., High-performance thermoacoustically driven triboelectric nanogenerator for autonomous wireless monitoring, Cell Reports Physical Science (2026), https://doi.org/10.1016/j.xcrp.2026.103214

triboelectric material owing to their strong charge affinity, good availability, and long-term durability. Copper functions both as the electropositive triboelectric layer and as the electrode in the HS-TENG. The cycle begins when the PTFE ball contacts the left copper electrode, as shown in Figure 2C<i>. At this moment, charge separation occurs due to triboelectrification and electrostatic induction,[48] resulting in the accumulation of negative charges on the PTFE ball and positive charges on the left copper electrode. As the PTFE ball moves away from the left copper electrode, a potential difference is formed between the left and right copper electrodes. Consequently, electrons move from the right electrode to the left electrode via the external circuit, generating an electric current, as illustrated in Figure 2C<ii>. As the cycle continues, the PTFE ball strikes the right copper electrode, leading to the accumulation of positive charges on the right copper electrode, as shown in Figure 2C<iii>. When the PTFE ball subsequently detaches from the right copper electrode, a new potential difference is established between the two electrodes, driving electrons from the left electrode to the right electrode and generating a current in the opposite direction, as depicted in Figure 2C<iv>. Driven by the TAO, the PTFE ball continuously reciprocates between the two electrodes, enabling repeated charge transfer and sustaining an alternating current (AC) within the external circuit.

The electrostatic field distribution of the HS-TENG is simulated by COMSOL Multiphysics, as shown in Figure 2D. The variations in potential observed during the four stages are in good agreement with the conceptual working mechanism illustrated in Figure 2C, thereby validating the explained charge transfer process. Based on the theory of freestanding contact-separation mode TENGs,[49] the governing equation for the HS-TENG can be written as,

$$V = -\frac{Q}{C} + V_{OC} = -\frac{(d_0+g)}{\varepsilon_0 S}Q + \frac{2\sigma x}{\varepsilon_0}, \qquad \text{(Equation 4)}$$

where Q, C, V_{OC}, d_0, g, ε_0, S, σ, and x are the transferred charge, the capacitance, the open-circuit voltage, the effective dielectric medium thickness, the total air gap between the two electrodes, the dielectric constant in vacuum, the effective contact area of the copper electrode layer, the charge density on the PTFE ball surface, and the separation distance between the electrode layer and the PTFE ball surface, respectively.

Thermal-to-acoustic energy conversion via TAO

To evaluate the performance of the proposed TADHS-TENG, the thermal-to-acoustic energy conversion characteristics of the TAO are first analyzed. When the temperature difference (ΔT) across the stack is above a critical value, the working gas (air) within the TAO transitions from a stationary state to self-excited oscillations, a phenomenon commonly referred to as thermoacoustic instability. In this work, a heat input of 48.4 W is applied to the HHE, while the CHE is cooled by circulating water, thereby establishing a significant temperature gradient along the stack. Figure S5A in the supplemental information illustrates the temporal evolution of the hot-end temperature (T_h), cold-end temperature (T_c), and their temperature difference ΔT ($=T_h$-T_c) when the left end of the TAO is sealed with only an elastic membrane under a tensile strain of ε = 0.4. At around 75 s, thermoacoustic instability occurs, corresponding to an onset temperature difference ΔT_{Onset} of 48°C. This results in a sudden increase in acoustic pressure amplitude, as shown in Figure S5B. It can be seen that the amplification of acoustic oscillations can be divided into three distinct phases: (1) the start-up phase, characterized by an exponential increase in pressure amplitude; (2) the saturation phase, where the growth of pressure amplitude slows down; and (3) the steady-state phase, exhibiting limit-cycle sinusoidal pressure oscillations with an amplitude p_{A0} of 26 Pa while the temperature difference ΔT_{Steady} stabilizes at 110°C. When the TAO is integrated with the HS-TENG, ΔT_{Onset} increases from 48°C to 80°C, and p_{A0} decreases from 26 to 10 Pa, as shown in Figures 3A and 3B. The changes in onset temperature and pressure amplitude are attributed to the increased effective acoustic mass, which brings about a larger equivalent acoustic resistance. Figure 3C further presents the frequency spectra of the time-history acoustic pressures shown in Figure 3B. Since the introduction of the HS-TENG increases the tensile strain of the membrane, the oscillation frequency of the TAO with the HS-TENG rises to 80.77 Hz, compared to 63.55 Hz without the HS-TENG.

To investigate the impact of the HS-TENG size on the performance of the TAO, HS-TENGs with different diameters d are fabricated. Figure 3D illustrates the effect of d on the onset temperature difference ΔT_{Onset} and oscillation frequency f. As d increases from 30 to 90 mm in increments of 10 mm, ΔT_{Onset} declines from 80°C to 49°C. Meanwhile, f decreases from 80.77 to 72.83 Hz due to the increased mass of the HS-TENG at larger diameters (refer to Figure S6 in the supplemental information), leading to a larger equivalent acoustic mass. The influence of d on the amplitudes of open-end pressure and membrane displacement is shown in Figure 3E. It is found that the pressure amplitude increases with increasing d, whereas the displacement amplitude shows an opposite trend. It could be inferred that the elastic membrane becomes stiffer as the HS-TENG diameter increases. Figures S7–S9 in the supplemental information further compare the open-circuit voltage, short-circuit current, and short-circuit charge of the TADHS-TENG with different diameters. The results indicate that the HS-TENG with a diameter d of 80 mm yields the highest electrical outputs. Therefore, d of 80 mm is chosen in the subsequent investigations on the influences of tensile strain ε and tube length L.

Figure 3F shows the influence of tensile strain ε on ΔT_{Onset} and f. An increase in ε gives rise to a larger effective stiffness, resulting in a lower ΔT_{Onset} and a higher f. The effect of ε on the amplitudes of open-end pressure and membrane displacement is illustrated in Figure 3G. As ε increases, the open-end pressure amplitude also rises due to the increased stiffness. However, the membrane displacement amplitude first increases and then decreases, reaching a peak value of 3.3 mm at ε = 0.4. The observed behavior is due to two contrasting effects: while a larger pressure amplitude promotes membrane deformation, a higher tensile strain makes the membrane stiffer and limits the deformation. As a result, a trade-off exists between the effects of increased pressure amplitude and tensile strain on membrane displacement.

Figure 3H illustrates the impact of tube length L on ΔT_{Onset} and f. As L increases, both ΔT_{Onset} and f decrease. The natural frequency f can be approximated by

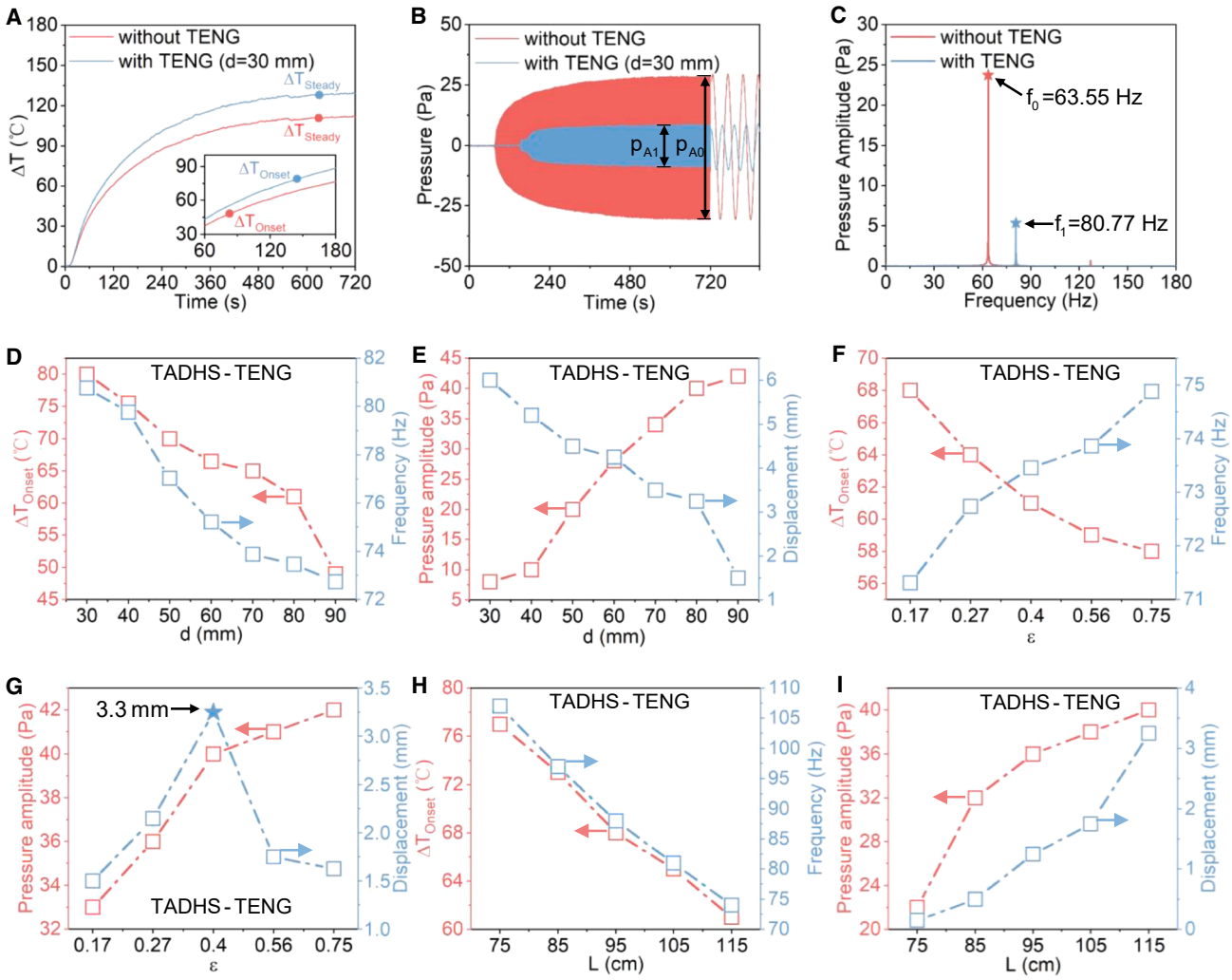

Figure 3. Performance evaluation of the thermoacoustic oscillator

(A) The time history of the temperature difference across the stack ends.
(B) The time history of the pressure at the open end of the resonator.
(C) Fast Fourier transform of the steady-state acoustic pressure.
(D) The effect of the HS-TENG diameter on the onset temperature difference and oscillation frequency.
(E) The effect of the HS-TENG diameter on the pressure amplitude and displacement amplitude.
(F) The effect of tensile strain on the onset temperature difference and oscillation frequency.
(G) The effect of tensile strain on the pressure amplitude and displacement amplitude.
(H) The effect of the tube length on the onset temperature difference and oscillation frequency.
(I) The effect of the tube length on the pressure amplitude and displacement amplitude.

$$f \approx \frac{a}{4L_{eff}}, \qquad \text{(Equation 5)}$$

where a is the sound speed. It can be seen that f is inversely proportional to the effective length L_{eff}. Swift[3] provided a rough estimate of the onset temperature gradient as follows:

$$\Delta T_{Onset} = \frac{\omega A |p_1|}{\rho_m c_p |U_1|}, \qquad \text{(Equation 6)}$$

where A, ρ_m, and c_p are the cross-section area, density, and isobaric heat capacity, respectively. Thus, a lower f often results in a smaller ΔT_{Onset}. Figure 3I shows the dependence of both open-end pressure amplitude and membrane displacement amplitude on L. It is found that both amplitudes increase with rising L. The increase in pressure amplitude is related to the reduced onset temperature difference, while the rise in displacement amplitude is attributed to both increased pressure amplitude and decreased oscillation frequency.

Acoustic-to-electric energy conversion via HS-TENG

Following the characterization of the TAO performance, the acoustic-to-electric energy conversion behavior of the HS-TENG is examined. The HS-TENG is designed to operate in

Please cite this article in press as: Chen et al., High-performance thermoacoustically driven triboelectric nanogenerator for autonomous wireless monitoring, Cell Reports Physical Science (2026), https://doi.org/10.1016/j.xcrp.2026.103214

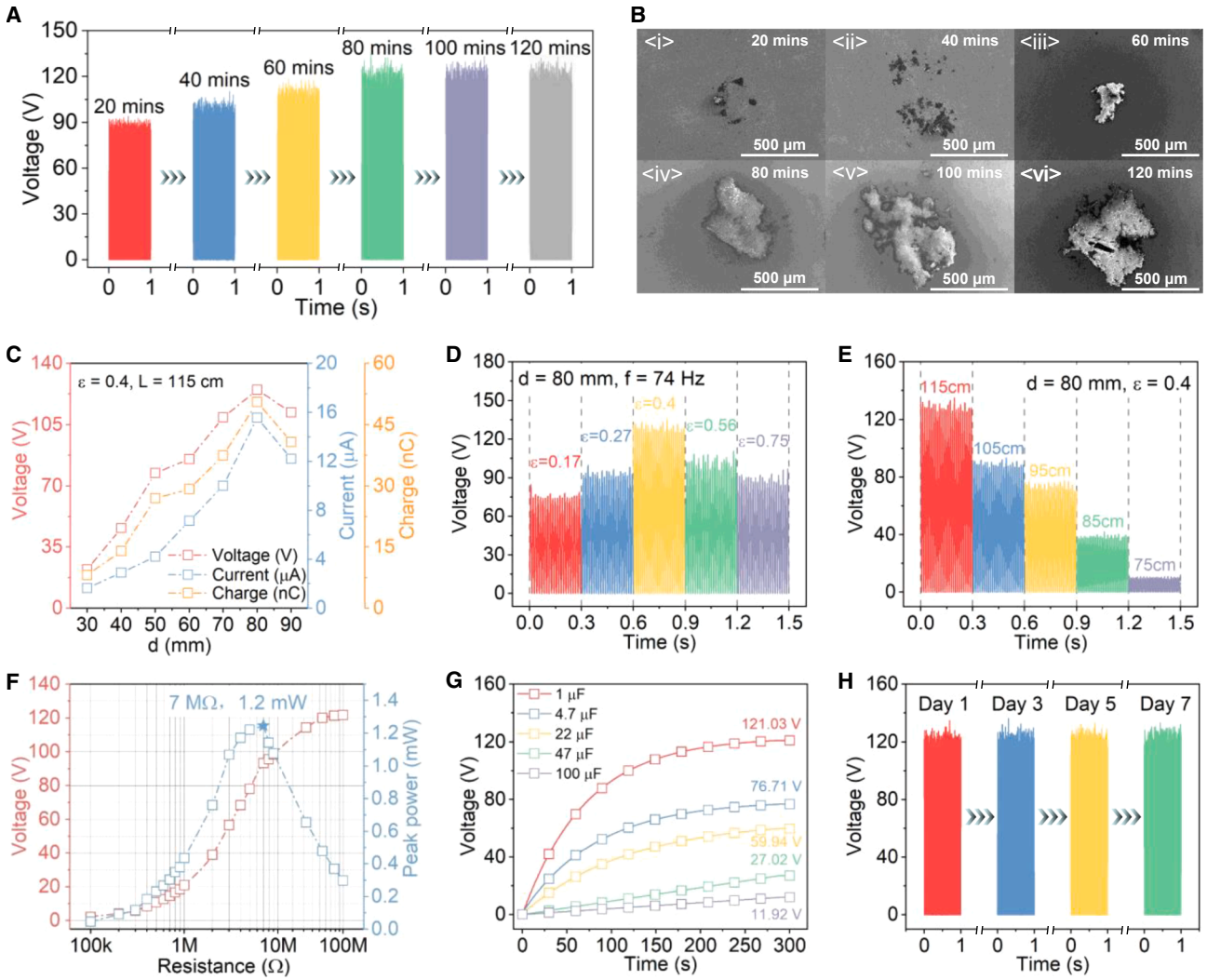

Figure 4. Performance evaluation of the TADHS-TENG

(A) Open-circuit voltage V_{OC} of the TADHS-TENG operating over different time intervals.

(B) SEM images of the copper film. Scale bars, 500 μm.

(C) The open-circuit voltage V_{OC}, short-circuit current I_{SC}, and short-circuit charge Q_{SC} at different diameters d.

(D) V_{OC} at different tensile strains ε with a fixed diameter d of 80 mm and tube length L of 115 cm.

(E) V_{OC} at different L with a fixed d of 80 mm and ε of 0.4.

(F) Dependence of voltage and instantaneous peak power on the external load resistance at a fixed d of 80 mm, ε of 0.71, and L of 115 cm.

(G) Charging histories of the TADHS-TENG for different capacitors.

(H) Voltage signals tested on different days.

the freestanding contact-separation mode between the two triboelectric layers. Therefore, its electrical output is influenced by the effective contact area and the contact force between the triboelectric layers. First, from the scanning electron microscopy (SEM) images in Figure S10 (supplemental information), we can see that there is no obvious abrasion on the PTFE balls before (**sub-image i**) and after (**sub-image ii**) usage. The unused copper film exhibits a smooth surface (**sub-image iii**), whereas a small area of abrasion appears after use for a while (**sub-image iv**). Moreover, the degree of abrasion varies with the operating time, resulting in different output performances. Figure 4A shows the open-circuit voltage output (V_{OC}) of the TADHS-TENG over time, with d fixed at 80 mm. In the first 80 min, the voltage output increases from 90 to 125 V and then remains almost constant. Figure 4B presents the SEM images of the copper film surface at different time intervals. Slight interface abrasion on the copper is visible in the first 60 min (**sub-images i**, **ii**, and **iii**), and after that, the abrasion becomes significant (**sub-images iv**, **v**, and **vi**). Combined with the results in Figure 4A, it can be inferred that the interface abrasion might increase the contact area between the PTFE balls and the copper film. Therefore, to determine their optimal output performance, the HS-TENG samples are operated for more than 80 min before

the subsequent measurements, and their performances are then compared, as shown in Figures 4C–4H.

Figure 4C illustrates the dependence of the open-circuit voltage V_{OC} (red line), short-circuit current I_{SC} (blue line), and short-circuit charge Q_{SC} (orange line) on the diameter d of the HS-TENG. When ε = 0.4 and L = 115 cm, as d varies from 30 to 80 mm, V_{OC} rises from 29.7 to 124.14 V, I_{SC} increases from 1.6 to 15.82 μA, and Q_{SC} grows from 8.31 to 50.54 nC. However, when d further increases to 90 mm, V_{OC}, I_{SC}, and Q_{SC} reduce to 76.88 V, 12.56 μA, and 31.85 nC, respectively. On one hand, as d increases, the number of PTFE balls increases, resulting in a larger contact area between the PTFE balls and copper film, which enhances electrical output. On the other hand, as d continues to increase, the increased mass of the HS-TENG leads to lower oscillation frequencies and smaller displacement amplitudes, which ultimately reduces electrical output. Hence, there is an optimal value of d at which the electrical output is maximized. We further examine the waveforms and RMS values of V_{OC}, I_{SC}, and Q_{SC} at steady state, as depicted in Figures S11A–S11C (supplemental information). It can be seen that V_{OC}, I_{SC}, and Q_{SC} exhibit sinusoidal patterns with non-zero RMS values, indicating the reliability and validity of the TADHS-TENG in generating electricity.

Figure 4D shows the dependence of V_{OC} on tensile strain ε and tube length L when d is fixed at 80 mm. V_{OC} first increases as ε rises from 0.17 to 0.4, then declines as ε further increases from 0.4 to 0.75. Similar trends can be observed in I_{SC} and Q_{SC}, as presented in Figures S12A and S12B in the supplemental information. Given a fixed number of PTFE balls, the amplitudes of V_{OC}, I_{SC}, and Q_{SC} exhibit a positive correlation with the collision force between the PTFE balls and the copper electrode layer. As shown in Figure S13A (supplemental information), the TADHS-TENG exhibits the highest acceleration when ε = 0.4, resulting in a stronger collision force. By fixing ε at 0.4, V_{OC}, I_{SC}, and Q_{SC} show a decreasing trend as L decreases from 115 to 75 cm, as shown in Figures 4E, S14A, and S14B (supplemental information). Although reducing the tube length leads to a higher frequency, the displacement amplitude decreases. As illustrated in Figure S13B (supplemental information), the HS-TENG achieves the highest acceleration when the tube length is set to 115 cm.

Figure 4F presents the dependence of V_{OC} (red line) and instantaneous peak power (blue line) on the external load resistance (adjusted via a rheostat box). It is found that when d, ε, and L are set to 80 mm, 0.4, and 115 cm, respectively, V_{OC} increases from nearly zero to 120 V as the external load resistance increases from 100 kΩ to 100 MΩ. Meanwhile, the instantaneous peak power initially increases and then decreases, reaching a maximum value of 1.2 mW at the optimal external load resistance of 7 MΩ. Figure S15 (supplemental information) shows that, at the optimal external load resistance, the RMS power is about 0.6 mW. Dividing this by the volume of the HS-TENG, which is 26.854×10^{-6} m^3, the instantaneous peak power and RMS power densities are calculated to be 44.6 and 22.3 W/m^3, respectively. The TADHS-TENG is further utilized to charge capacitors with different capacitances (1, 4.7, 10, 47, and 100 μF), and the voltage charging curves are displayed in Figure 4G. It shows that within 300 s, the voltages across those capacitors increase from 0 to 121.03, 76.71, 59.94, 27.02, and 11.92 V, respectively. To assess its robustness, the TADHS-TENG is tested for 7 consecutive days, and the voltage signals are illustrated in Figure 4H. It is found that the TADHS-TENG consistently delivers stable voltage outputs, demonstrating its high durability and reliability as a long-term energy harvesting solution.

Application demonstration of the TADHS-TENG

After separately characterizing the energy conversion behavior of the TAO and the HS-TENG, the feasibility and application potential of the proposed TADHS-TENG as a sustainable power source for low-power wireless sensing systems are explored. Since the TADHS-TENG delivers an AC output and its high internal resistance (7 MΩ) limits effective capacitor charging, it is essential to first incorporate a rectification circuit for AC-to-DC conversion, then use a PMM to enhance the efficiency, as shown in Figure 5A.

Figure 5B shows the instantaneous peak power of the TADHS-TENG with and without using the PMM when d, ε, and L are fixed at 80 mm, 0.4, and 115 cm, respectively. Without the PMM, the peak power is about 1.2 mW at an optimal resistance of 7 MΩ, whereas with the PMM integrated, the peak power decreases to 0.82 mW at a significantly lower optimal resistance of 200 kΩ. Although using the PMM reduces peak power, it lowers the internal resistance of the TADHS-TENG and enhances the DC output, as shown in Figure S16 (supplemental information). Moreover, the PMM improves the capacitor charging speed by mitigating the impedance mismatch between the TADHS-TENG and the capacitor, as shown in Figure 5C. Specifically, when the TADHS-TENG without a PMM is used to charge a 68 μF capacitor, the voltage increases from 0 to 11.26 V in 200 s. In contrast, with the PMM integrated, the voltage rises to 42.84 V in the same time period, firmly demonstrating the effectiveness of the PMM in significantly enhancing the capacitor charging speed. Furthermore, as shown in Figure 5D, after integrating the PMM, capacitors of various values can be easily charged to over 5 V, meeting the voltage requirement for operating the wireless sensor node explored in the following section. In addition to charging the capacitors, the TADHS-TENG can be used to power LEDs. Figure 5E shows 150 LEDs connected in series to form the pattern "SEU" (Southeast University) lit up by the TADHS-TENG. Figure S17 and Video S1 in the supplemental information further show that the TADHS-TENG can effortlessly power over 300 LEDs, highlighting its promising potential as a sustainable power source for low-power electronics.

Based on the excellent output performance of the TADHS-TENG presented above, a low-power wireless sensor node is designed to showcase its practical application. Integrated with the TADHS-TENG and solely powered by it, a self-sustained real-time temperature monitoring system is realized. The test bench for the TADHS-TENG-powered wireless sensor node is illustrated in Figure 5F. First, artificial thermal energy (about 48.4 W) from heating rods is transformed into acoustic energy through the TAO, which is subsequently converted into electrical energy through the TADHS-TENG. Second, the electricity generated by the TADHS-TENG powers the circuit board that integrates a rectifier, a PMM (with a 68 μF storage capacitor used), an energy

Please cite this article in press as: Chen et al., High-performance thermoacoustically driven triboelectric nanogenerator for autonomous wireless monitoring, Cell Reports Physical Science (2026), https://doi.org/10.1016/j.xcrp.2026.103214

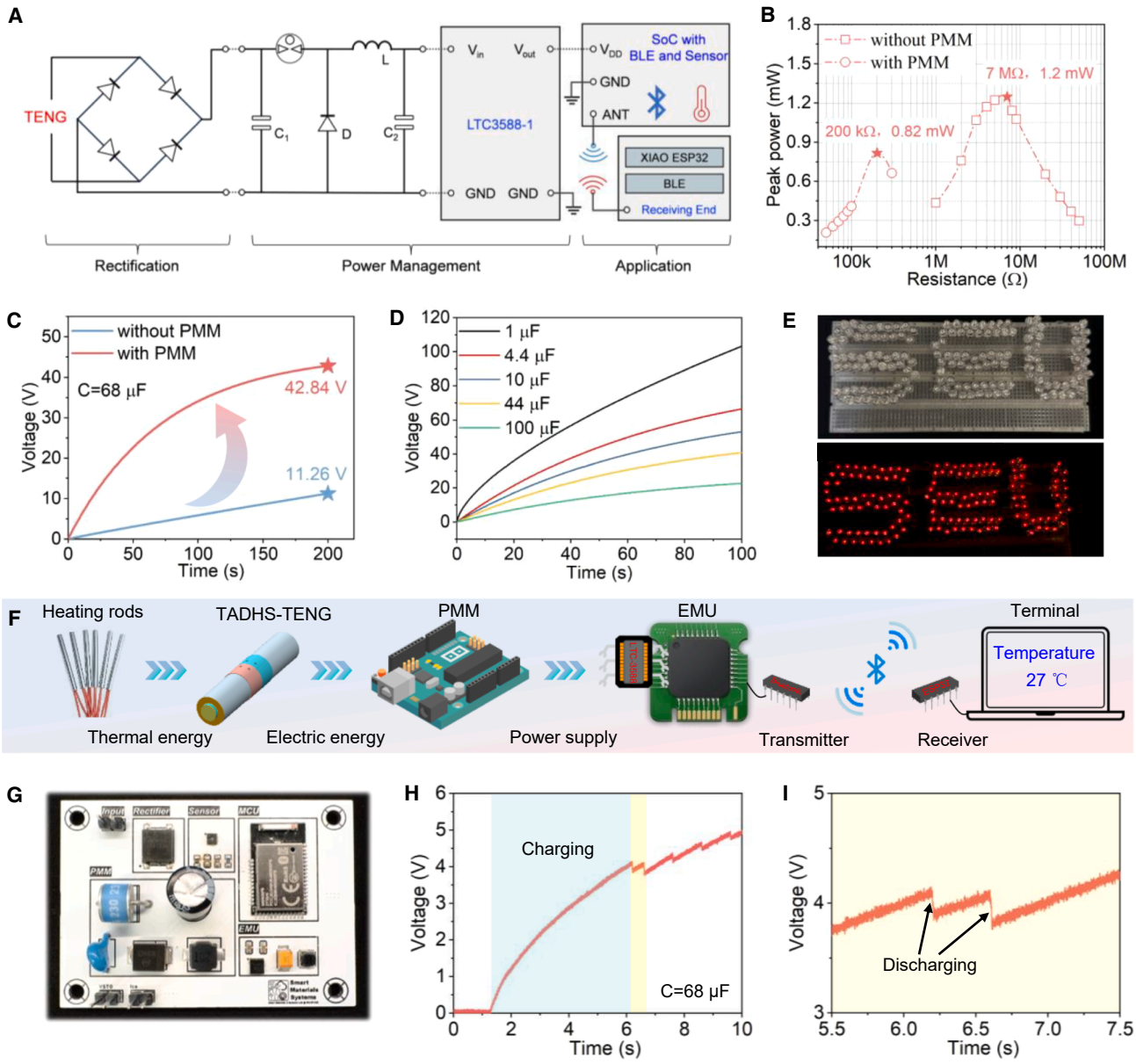

Figure 5. Demonstration of a TADHS-TENG-powered wireless monitoring system

(A) Schematic of the circuit.

(B) Instantaneous peak power of the TADHS-TENG with and without using the PMM.

(C) Voltage charging history of the storage capacitor (68 μF) with and without the PMM, highlighting the enhancement of the PMM in charging performance.

(D) Voltage charging speed of capacitors with different values using the TADHS-TENG integrated with PMM.

(E) Photograph of 150 LEDs arranged in the pattern "SEU" and powered by the TADHS-TENG.

(F) Test bench for the TADHS-TENG-powered wireless sensing system.

(G) Photograph of the fabricated circuit board integrating the wireless sensor node.

(H) Voltage profile of the storage capacitor (68 μF) during the operation of the self-powered wireless sensing system.

(I) Enlarged view of the discharging phase.

management unit (EMU), and a wireless sensing node comprising a microcontroller (MCU) and a temperature sensor. The EMU, realized using an LTC3588-1 chip, serves as a core component of the circuit board that enables the functioning of the wireless sensing node. It features an ultralow quiescent current of only 950 nA. Moreover, the EMU is specifically chosen for its undervoltage lockout (UVLO) function, which features a wide hysteresis window and plays a critical role in system operation. This function enables the gradual accumulation of energy from the TADHS-TENG. Once sufficient energy is stored, the EMU

delivers a stable output to the user-end components. The MCU remains powered off most of the time to save energy and only activates when a stabilized voltage is provided (see the analysis of power consumption in the methods section). Upon activation, it controls the sensor to measure ambient temperature and transmits the data via Bluetooth low energy (BLE). The received data are then uploaded to the cloud server and are accessible anywhere on any terminal. A photograph of the fabricated circuit board integrating the wireless sensor node is shown in Figure 5G.

Figure 5H shows the voltage variation of the storage capacitor (68 μF) during the operation of the self-powered wireless sensing system, where multiple charging and discharging cycles are observed. In the first charging process, the capacitor stores energy harvested by the TADHS-TENG, with its voltage rising from 0 to 4.2 V within only 6 s. Then, the capacitor releases energy to power the wireless sensor node through the voltage regulator LTC3588-1. The voltage drops from 4.2 to 3.8 V in 0.4 s during this discharging process, as illustrated in Figure 5I. This charging-discharging cycle repeats until the voltage reaches 5 V at 10 s. Video S2 in the supplemental information provides a detailed demonstration of the whole self-powered sensing process.

DISCUSSION

This paper presents a TADHS-TENG as a novel technology for self-powered wireless monitoring. The proposed TADHS-TENG combines a TAO, which converts heat into acoustic energy, and an HS-TENG, which converts acoustic energy into electricity. Experiments are conducted to optimize the performance of the TADHS-TENG by varying the HS-TENG diameter d, membrane tensile strain ε, and tube length L. To showcase the application potential of the TADHS-TENG, it is utilized to power LEDs and a custom-designed wireless sensor. The primary findings of this work are summarized as follows.

Firstly, the performance of the TADHS-TENG proposed in this study is superior to that of the previously reported thermoacoustically driven triboelectric nanogenerators. Experimental results demonstrate that, with d = 80 mm, ε = 0.71, L = 115 cm, and given a heat input of 48.4 W, the TADHS-TENG achieves a maximum open-circuit voltage of 124.14 V (RMS: 76.88 V), a peak short-circuit current of 15.82 μA (RMS: 12.02 μA), and a maximum short-circuit charge of 50.54 nC (RMS: 31.85 nC). Under the impedance-matching condition, the TADHS-TENG produces a maximum instantaneous peak power of 1.2 mW, corresponding to a power density of 44.6 W/m^3, at an optimal load resistance of 7 MΩ. Secondly, the integration of a PMM can significantly reduce the internal resistance of the TADHS-TENG from 7 MΩ to 200 kΩ, thereby enhancing the current output and capacitor charging efficiency. Specifically, when integrated with a PMM, the TADHS-TENG can generate a peak short-circuit current of 65.37 μA and power more than 300 LEDs. In addition, it can charge a 100 μF capacitor from 0 to 20 V within 100 s. Finally, the TADHS-TENG developed in this study has been successfully used to power a custom-designed temperature sensor node. The results show that the TADHS-TENG can charge the capacitor voltage to 4.2 V in just 6 s, after which the energy is regulated by an EMU to power the wireless sensor node continuously over the next 4 s tested in the experiment.

Overall, despite its low thermal-to-electric efficiency, the TADHS-TENG proposed in this study exhibits superior electrical performance metrics, including maximum output voltage, peak current, total charge transfer, and instantaneous peak power, making it well-suited for thermal energy harvesting and for powering low-power electronic devices. Future work may focus on utilizing other highly efficient TAOs, such as traveling wave ones, to enhance the thermal-to-acoustic energy conversion efficiency. Additionally, optimization in terms of the TENG structure (such as replacing copper films with electroplated copper electrodes) can be explored to further improve the electrical output.

METHODS

Fabrication of the TADHS-TENG

The TADHS-TENG tested in the experiments comprises two main components: a TAO and an HS-TENG. The TAO consists of a hot buffer, a stack, a pair of heat exchangers (hot and cold), and a resonator. The hot buffer is made of a quartz tube to withstand high temperatures, and the thickness of the quartz tube is 3 mm. The left end of the hot buffer is sealed with an elastic membrane, while the right end is connected to the hot heat exchanger. Sandwiched between the HHE and the CHE is the stack, made of ceramics with a primary composition of Al_2O_3. The stack adopts a honeycomb structure consisting of numerous square channels with dimensions of 1.8 mm × 1.8 mm and a total length of 20 mm. To enhance thermal contact, copper mesh screens are inserted between the stack and the heat exchangers, which are secured together via thread connections. Additionally, both the HHE and CHE contain two channels on surfaces, oriented perpendicular to the axial direction, each with a diameter of 8.5 mm. In the HHE, these channels house the heating rods, whereas in the CHE, they serve for circulating cooling water. Finally, the left end of the TAO is connected to the CHE, while the right end is open, allowing sound waves to radiate into the surrounding environment.

The HS-TENG consists of a honeycomb frame, PTFE balls, two copper electrode layers, and two substrate plates. The honeycomb frame and substrate plates are fabricated using an FDM 3D printer (Bambu X1 Carbon) with PLA filament. The honeycomb structure has a diameter d varying from 30 to 90 mm, in increments of 10 mm. Circular grooves with a diameter of 3.5 mm are distributed throughout the frame, each housing a PTFE ball with a diameter of 3 mm. The grooves are arranged in a regular hexagonal pattern, with a wall thickness of 1 mm between the adjacent grooves, to maximize the number of PTFE balls that can be accommodated. This configuration increases the contact area between the PTFE balls and electrode layers, thereby enhancing the electrical output. The PTFE balls are inserted into the honeycomb frame, which is then sandwiched between the two substrate plates affixed with copper electrodes. Finally, an elastic membrane is used to seal the left end of the hot buffer, and the HS-TENG is affixed to the membrane, completing the assembly of the TADHS-TENG. Detailed information on the geometrical dimensions of the TADHS-TENG can be found in Table S2 (supplemental information).

Experimental measurements

To monitor the operating condition of the TADHS-TENG, multiple measurement instruments were utilized in this study. Firstly, two K-type thermocouples (GG-K-36-SLE, resolution 0.75%) were affixed to the outer surfaces of the HHE and CHE to monitor the real-time temperature at the two ends of the stack. A data acquisition (DAQ) module (NI 9212, National Instruments) was used to collect and record the temperature data. Secondly, an acoustic microphone (GRAS, 46BD-FV), with a sensitivity of 1.4 mV/Pa at 250 Hz (±3 dB), was placed at the open end to capture pressure variation inside the TAO. Prior to measurements, the microphone was calibrated using a GRAS 42AG multifunction sound calibrator to ensure reliable and accurate data acquisition. The NI 9230 DAQ module was used to take the acoustic pressure signal from the microphone. Both NI 9212 and NI 9230 cards were operated using NI DAQ Express software for real-time monitoring. Thirdly, a Doppler laser displacement sensor (SG6150) was employed to measure the displacement amplitude of the elastic membrane. The laser beam from the sensor was directed at the center of the elastic membrane to enable non-contact measurement of its displacement during operation. Note that a zero-point calibration of the laser displacement sensor was conducted before measurement. Finally, an electrometer (Keithley 6514) was used to measure the electrical outputs, including the V_{OC}, I_{SC}, and Q_{SC}. For the TADHS-TENG without a PMM, the electrometer was connected directly to the TENG electrodes, whereas for the TADHS-TENG with a PMM, it was connected to the capacitor.

Theoretical modeling of the TADHS-TENG

Following experimental investigations, a system-level reduced-order network model of the TADHS-TENG was developed. In the theoretical framework, it is discretized into multiple thermoacoustic elements, each represented by a ''five-parameter'' impedance model derived from linear thermoacoustic theory. By employing the acoustic-electric analogy, the entire system is mapped onto an equivalent electrical circuit. This network model enables the prediction of key onset characteristics, including the onset temperature and oscillation frequency. A comparison between theoretical predictions and experimental results demonstrates strong agreement, thereby validating the accuracy of the proposed model. Details of the derivation process are provided in Note S1 (supplemental information).

Power consumption of the sensing node

The average power consumption was characterized using a precision power analyzer under the condition of a regulated supply voltage of 3.3 V. As shown in the measured current waveform in Figure S18 (supplemental information), the wireless sensing node operates in a duty-cycled manner, featuring short high-current bursts during data transmission and ultra-low current during standby periods. The measured peak current reaches approximately 13.15 mA, while the average current over a 1 s time window is 98.67 μA, corresponding to an average power consumption of approximately 0.33 mW.

RESOURCE AVAILABILITY

Lead contact

Requests for further information and resources should be directed to and will be fulfilled by the lead contact, Guobiao Hu (guobiaohu@hkust-gz.edu.cn).

Materials availability

This study did not generate new, unique reagents.

Data and code availability

- Raw data underlying the study are available from the lead contact upon request.
- This paper does not report original code.
- Any additional information required to reanalyze the data reported in this paper is available from the lead contact upon request.

ACKNOWLEDGMENTS

This work was financially supported by the National Natural Science Foundation of China (grant nos. 52405096 and 52305135), the Natural Science Foundation of Jiangsu Province (grant no. BK20230848), the Guangdong Provincial Project (grant no. 2023QN10L545), Zhishan Young Scholar Program of Southeast University (grant no. 2242025RCB0037), and Nansha District Science and Technology Project (grant no. 2024ZD008).

AUTHOR CONTRIBUTIONS

Conceptualization, software, formal analysis, methodology, funding acquisition, and writing – original draft, G.C.; software, formal analysis, and methodology, Y.W.; software, formal analysis, and methodology, S.T.; writing – review & editing, J.X.; writing – review & editing, L.T.; writing – review & editing, J.W.; funding acquisition, supervision, and writing – review & editing, G.H.; and funding acquisition and writing – review & editing, A.D.

DECLARATION OF INTERESTS

The authors declare that they have no conflict of interest.

SUPPLEMENTAL INFORMATION

Supplemental information can be found online at https://doi.org/10.1016/j.xcrp.2026.103214.

Received: November 23, 2025
Revised: February 2, 2026
Accepted: February 27, 2026

REFERENCES

1. Chu, S., and Majumdar, A. (2012). Opportunities and challenges for a sustainable energy future. Nature *488*, 294–303. https://doi.org/10.1038/nature11475.
2. Backhaus, S., and Swift, G.W. (1999). A thermoacoustic Stirling heat engine. Nature *399*, 335–338. https://doi.org/10.1038/20624.
3. Swift, G.W. (2017). Thermoacoustics, A Unifying Perspective for Some Engines and Refrigerators (Springer).
4. Maddi, A., Olivier, C., Poignand, G., Penelet, G., Pagneux, V., and Aurégan, Y. (2023). Frozen sound: An ultra-low frequency and ultra-broadband non-reciprocal acoustic absorber. Nat. Commun. *14*, 4028. https://doi.org/10.1038/s41467-023-39727-4.
5. Chen, G., Tang, L., Mace, B., and Yu, Z. (2021). Multi-physics coupling in thermoacoustic devices: A review. Renew. Sustain. Energy Rev. *146*, 111170. https://doi.org/10.1016/j.rser.2021.111170.

6. Chen, Y., Yu, G., Chen, Y., Zhu, S., Luo, J., Sun, Y., and Luo, E. (2024). Post-positioned gas spring enables ultra-high output power of hybrid thermoacoustic electric generators. Cell Rep. Phys. Sci. *5*, 101835. https://doi.org/10.1016/j.xcrp.2024.101835.

7. Xiao, L., Luo, K., Wu, Z., Chi, J., Xu, J., Zhang, L., Hu, J., and Luo, E. (2024). A highly efficient heat-driven thermoacoustic cooling system. Cell Rep. Phys. Sci. *5*, 101815. https://doi.org/10.1016/j.xcrp.2024.101815.

8. Huang, J., Yang, R., Yang, Y., Zhou, Q., and Luo, E. (2023). Generalized thermoacoustic heat engines with unconventional working substances: A review. Appl. Energy *347*, 121447. https://doi.org/10.1016/j.apenergy.2023.121447.

9. Biwa, T., Watanabe, T., and Penelet, G. (2020). Flywheel-based traveling-wave thermoacoustic engine. Appl. Phys. Lett. *117*, 243902. https://doi.org/10.1063/5.0022315.

10. Wang, K., Dubey, S., Choo, F.H., and Duan, F. (2017). Thermoacoustic Stirling power generation from LNG cold energy and low-temperature waste heat. Energy *127*, 280–290. https://doi.org/10.1016/j.energy.2017.03.124.

11. Wu, Z., Yu, G., Zhang, L., Dai, W., and Luo, E. (2014). Development of a 3kW double-acting thermoacoustic Stirling electric generator. Appl. Energy *136*, 866–872. https://doi.org/10.1016/j.apenergy.2014.04.105.

12. Zhu, S., Wang, T., Jiang, C., Wu, Z., Yu, G., Hu, J., Markides, C.N., and Luo, E. (2023). Experimental and numerical study of a liquid metal magnetohydrodynamic generator for thermoacoustic power generation. Appl. Energy *348*, 121453. https://doi.org/10.1016/j.apenergy.2023.121453.

13. Chen, G., Tao, S., Liang, R., Li, Z., Sun, W., Xu, J., and Yu, Z. (2024). Development of a sunlight-driven thermoacoustic engine for solar energy harvesting. Appl. Therm. Eng. *238*, 122047. https://doi.org/10.1016/j.applthermaleng.2023.122047.

14. Kang, H., Cheng, P., Yu, Z., and Zheng, H. (2015). A two-stage traveling-wave thermoacoustic electric generator with loudspeakers as alternators. Appl. Energy *137*, 9–17. https://doi.org/10.1016/j.apenergy.2014.09.090.

15. Chen, G., Tang, L., and Mace, B.R. (2019). Modelling and analysis of a thermoacoustic-piezoelectric energy harvester. Appl. Therm. Eng. *150*, 532–544. https://doi.org/10.1016/j.applthermaleng.2019.01.025.

16. Nouh, M., Aldraihem, O., and Baz, A. (2014). Theoretical modeling and experimental realization of dynamically magnified thermoacoustic-piezoelectric energy harvesters. J. Sound Vib. *333*, 3138–3152. https://doi.org/10.1016/j.jsv.2014.02.016.

17. Zheng, Y., Wang, W., Niu, J., Jin, X., Sun, Y., Peng, L., Li, W., Wang, H., and Lin, T. (2022). Thermoacoustic energy harvesting using thermally-stabilized polyacrylonitrile nanofibers. Nano Energy *95*, 106995. https://doi.org/10.1016/j.nanoen.2022.106995.

18. Matveev, K.I., Wekin, A., Richards, C.D., and Shafrei-Tehrany, N. (2007). On the coupling between standing-wave thermoacoustic engine and piezoelectric transducer. ASME 2007 International Mechanical Engineering Congress and Exposition, 765-769. https://doi.org/10.1115/IMECE2007-41119.

19. Smoker, J., Nouh, M., Aldraihem, O., and Baz, A. (2012). Energy harvesting from a standing wave thermoacoustic-piezoelectric resonator. J. Appl. Phys. *111*, 104901. https://doi.org/10.1063/1.4712630.

20. Zhao, D. (2013). Waste thermal energy harvesting from a convection-driven Rijke–Zhao thermo-acoustic-piezo system. Energy Convers. Manag. *66*, 87–97. https://doi.org/10.1016/j.enconman.2012.09.025.

21. Wu, C., Wang, A.C., Ding, W., Guo, H., and Wang, Z.L. (2018). Triboelectric Nanogenerator: A Foundation of the Energy for the New Era. Adv. Energy Mater. *9*, 1802906. https://doi.org/10.1002/aenm.201802906.

22. Wang, Y., Du, H., Yang, H., Xi, Z., Zhao, C., Qian, Z., Chuai, X., Peng, X., Yu, H., Zhang, Y., et al. (2024). A rolling-mode triboelectric nanogenerator with multi-tunnel grating electrodes and opposite-charge-enhancement for wave energy harvesting. Nat. Commun. *15*, 6834. https://doi.org/10.1038/s41467-024-51245-5.

23. Wu, H., Shan, C., Fu, S., Li, K., Wang, J., Xu, S., Li, G., Zhao, Q., Guo, H., and Hu, C. (2024). Efficient energy conversion mechanism and energy storage strategy for triboelectric nanogenerators. Nat. Commun. *15*, 6558. https://doi.org/10.1038/s41467-024-50978-7.

24. Xia, K., Zhu, Z., Zhang, H., Du, C., Wang, R., and Xu, Z. (2018). Cost-effective triboelectric nanogenerator based on teflon tape and conductive copper foil tape. Microelectron. Eng. *199*, 114–117. https://doi.org/10.1016/j.mee.2018.08.002.

25. Li, T., Xu, Y., Willander, M., Xing, F., Cao, X., Wang, N., and Wang, Z.L. (2016). Lightweight triboelectric nanogenerator for energy harvesting and sensing tiny mechanical motion. Adv. Funct. Mater. *26*, 4370–4376. https://doi.org/10.1002/adfm.201600279.

26. Peng, F., Liu, D., Zhao, W., Zheng, G., Ji, Y., Dai, K., Mi, L., Zhang, D., Liu, C., and Shen, C. (2019). Facile fabrication of triboelectric nanogenerator based on low-cost thermoplastic polymeric fabrics for large-area energy harvesting and self-powered sensing. Nano Energy *65*, 104068. https://doi.org/10.1016/j.nanoen.2019.104068.

27. Xia, K., and Xu, Z. (2021). Applying a triboelectric nanogenerator by using facial mask for flexible touch sensor. Sensor Actuator Phys. *331*, 112710. https://doi.org/10.1016/j.sna.2021.112710.

28. Jiang, T., Pang, H., An, J., Lu, P., Feng, Y., Liang, X., Zhong, W., and Wang, Z.L. (2020). Robust Swing-Structured Triboelectric Nanogenerator for Efficient Blue Energy Harvesting. Adv. Energy Mater. *10*, 2000064. https://doi.org/10.1002/aenm.202000064.

29. Zi, Y., Wu, C., Ding, W., Wang, X., Dai, Y., Cheng, J., Wang, J., Wang, Z., and Wang, Z.L. (2018). Field Emission of Electrons Powered by a Triboelectric Nanogenerator. Adv. Funct. Mater. *28*, 1800610. https://doi.org/10.1002/adfm.201800610.

30. Gong, S., Li, K., Sun, J., Chen, J., and Guo, H. (2025). Interfacial droplet-based triboelectric nanogenerator with optimized architecture for highly efficient vibrational energy conversion. Joule *9*, 101763. https://doi.org/10.1016/j.joule.2024.09.010.

31. Dong, L., Hu, G., Tang, Q., Zhao, C., Yang, F., and Yang, Y. (2024). Advanced Aerodynamics-Driven Energy Harvesting Leveraging Galloping-Flutter Synergy. Adv. Funct. Mater. *35*, 2414324. https://doi.org/10.1002/adfm.202414324.

32. Zhao, C., Hu, G., and Yang, Y. (2022). A cantilever-type vibro-impact triboelectric energy harvester for wind energy harvesting. Mech. Syst. Signal Process. *177*, 109185. https://doi.org/10.1016/j.ymssp.2022.109185.

33. Wang, Y., Cai, S., Wang, Y., Wu, D., Xiang, G., Yang, S., Zhang, J., Dai, S., Xu, M., and Xiang, X. (2024). Study on dynamics and power generation performance coupling of galloping-based triboelectric nanogenerator for harvesting broadband wind energy. Nano Energy *130*, 110126. https://doi.org/10.1016/j.nanoen.2024.110126.

34. Jiang, T., Yao, Y., Xu, L., Zhang, L., Xiao, T., and Wang, Z.L. (2017). Spring-assisted triboelectric nanogenerator for efficiently harvesting water wave energy. Nano Energy *31*, 560–567. https://doi.org/10.1016/j.nanoen.2016.12.004.

35. Zhang, C., Hao, Y., Yang, J., Su, W., Zhang, H., Wang, Z.l., Wang, J., and Li, X. (2025). Magnetic suspension damped hybrid nanogenerator for water wave energy harvesting. Adv. Energy Mater. *15*, 2500130. https://doi.org/10.1002/aenm.202500130.

36. Jiang, T., Zhang, L.M., Chen, X., Han, C.B., Tang, W., Zhang, C., Xu, L., and Wang, Z.L. (2015). Structural optimization of triboelectric nanogenerator for harvesting water wave energy. ACS Nano *9*, 12562–12572. https://doi.org/10.1021/acsnano.5b06372.

37. Fan, X., Chen, J., Yang, J., Bai, P., Li, Z., and Wang, Z.L. (2015). Ultrathin, rollable, paper-based triboelectric nanogenerator for acoustic energy harvesting and self-powered sound recording. ACS Nano *9*, 4236–4243. https://doi.org/10.1021/acsnano.5b00618.

38. Zhao, H., Xiao, X., Xu, P., Zhao, T., Song, L., Pan, X., Mi, J., Xu, M., and Wang, Z.L. (2019). Dual-Tube Helmholtz Resonator-Based Triboelectric Nanogenerator for Highly Efficient Harvesting of Acoustic Energy. Adv. Energy Mater. *9*, 1902824. https://doi.org/10.1002/aenm.201902824.

39. Zhang, Y., Lai, S.-K., Wang, C., Ho, K.-F., and Wang, C.H. (2025). Acoustic energy boosts air purification: A novel sound-wave drive TENG for filterless particulate capturing. Nano Energy *135*, 110674. https://doi.org/10.1016/j.nanoen.2025.110674.

40. Zhang, C., Hao, Y., Lu, X., Su, W., Zhang, H., Wang, Z.L., and Li, X. (2025). Advances in TENGs for marine energy harvesting and in situ electrochemistry. Nano-Micro Lett. *17*, 124. https://doi.org/10.1007/s40820-024-01640-w.

41. Zeng, Q., Luo, Y., Zhang, X., Tan, L., Chen, A., Tang, Q., Yang, H., and Wang, X. (2023). A Bistable Triboelectric Nanogenerator for Low-Grade Thermal Energy Harvesting and Solar Thermal Energy Conversion. Small *19*, 2301952. https://doi.org/10.1002/smll.202301952.

42. Fu, J., Xu, G., Li, C., Xia, X., Guan, D., Li, J., Huang, Z., and Zi, Y. (2020). Achieving Ultrahigh Output Energy Density of Triboelectric Nanogenerators in High-Pressure Gas Environment. Adv. Sci. *7*, 2001757. https://doi.org/10.1002/advs.202001757.

43. Zhou, L., Liu, D., Zhao, Z., Li, S., Liu, Y., Liu, L., Gao, Y., Wang, Z.L., and Wang, J. (2020). Simultaneously Enhancing Power Density and Durability of Sliding-Mode Triboelectric Nanogenerator via Interface Liquid Lubrication. Adv. Energy Mater. *10*, 2002920. https://doi.org/10.1002/aenm.202002920.

44. He, W., Liu, W., Chen, J., Wang, Z., Liu, Y., Pu, X., Yang, H., Tang, Q., Yang, H., Guo, H., and Hu, C. (2020). Boosting output performance of sliding mode triboelectric nanogenerator by charge space-accumulation effect. Nat. Commun. *11*, 4277. https://doi.org/10.1038/s41467-020-18086-4.

45. Long, L., Liu, W., Wang, Z., He, W., Li, G., Tang, Q., Guo, H., Pu, X., Liu, Y., and Hu, C. (2021). High performance floating self-excited sliding triboelectric nanogenerator for micro mechanical energy harvesting. Nat. Commun. *12*, 4689. https://doi.org/10.1038/s41467-021-25047-y.

46. Qu, J., Yuan, Q., Li, Z., Wang, Z., Xu, F., Fan, Q., Zhang, M., Qian, X., Wang, X., Wang, X., and Xu, M. (2023). All-in-one strain-triboelectric sensors based on environment-friendly ionic hydrogel for wearable sensing and underwater soft robotic grasping. Nano Energy *111*, 108387. https://doi.org/10.1016/j.nanoen.2023.108387.

47. Wang, S., Xie, Y., Niu, S., Lin, L., and Wang, Z.L. (2014). Freestanding triboelectric-layer-based nanogenerators for harvesting energy from a moving object or human motion in contact and non-contact modes. Adv. Mater. *26*, 2818–2824. https://doi.org/10.1002/adma.201305303.

48. Jiang, T., Chen, X., Han, C.B., Tang, W., and Wang, Z.L. (2015). Theoretical Study of Rotary Freestanding Triboelectric Nanogenerators. Adv. Funct. Mater. *25*, 2928–2938. https://doi.org/10.1002/adfm.201500447.

49. Niu, S., Liu, Y., Chen, X., Wang, S., Zhou, Y.S., Lin, L., Xie, Y., and Wang, Z.L. (2015). Theory of freestanding triboelectric-layer-based nanogenerators. Nano Energy *12*, 760–774. https://doi.org/10.1016/j.nanoen.2015.01.013.

50. Zhu, S., Yu, A., Yu, G., Liu, Y., Zhai, J., Dai, W., and Luo, E. (2017). Thermoacoustically driven triboelectric nanogenerator: Combining thermoacoustics and nanoscience. Appl. Phys. Lett. *111*, 153901. https://doi.org/10.1063/1.4999284.

51. Ahmed, F., Yu, G., and Luo, E. (2023). A triboelectric nanogenerator attached to a thermoacoustic heat engine for power generation. Energy Convers. Manag. *276*, 116482. https://doi.org/10.1016/j.enconman.2022.116482.

52. Zhu, S., Yu, G., Tang, W., Hu, J., and Luo, E. (2021). Thermoacoustically driven liquid-metal-based triboelectric nanogenerator: A thermal power generator without solid moving parts. Appl. Phys. Lett. *118*, 113902. https://doi.org/10.1063/5.0041415.

53. Xia, K., and Yu, M. (2025). Highly robust and efficient metal-free water cup solid–liquid triboelectric nanogenerator for water wave energy harvesting and ethanol detection. Chem. Eng. J. *503*, 157938. https://doi.org/10.1016/j.cej.2024.157938.

54. Xia, K., Yu, M., Luo, Y., and Ding, Y. (2025). All-foam intrinsic triboelectric static and dynamic pressure sensor with a standardized DC/AC measurement method for industrial robots. Nano Energy *139*, 110953. https://doi.org/10.1016/j.nanoen.2025.110953.

55. Xia, K., Hao, Y., Luo, P., Zhang, Y., Guo, J., and Zhu, Z. (2025). A Faraday Cage-Inspired Triboelectric Nanogenerator Enabled by Alloy Powder Architecture for Self-Powered Ocean Sensing. Energy &. Environ. Materials *8*, e70040. https://doi.org/10.1002/eem2.70040.

56. Wen, J., Zhang, L., Kang, H., Liu, S., and Wang, K. (2024). Advances in the utilization and suppression of thermoacoustic effect: A review. Int. J. Heat Mass Tran. *231*, 125758. https://doi.org/10.1016/j.ijheatmasstransfer.2024.125758.